The Two-Dimensional Evolution of Thermospheric $\sum$O/N$_2$ Response to Weak Geomagnetic Activity During Solar-Minimum Observed by GOLD

Xuguang Cai[1] (ID), Alan G. Burns[1] (ID), Wenbin Wang[1] (ID), Liying Qian[1] (ID), Stanley C. Solomon[1] (ID), Richard W. Eastes[2] (ID), Nicholas Pedatella[1], Robert E. Daniell[3], and William E. McClintock[2] (ID)

[1]High Altitude Observatory, National Center for Atmospheric Research, Boulder, CO, USA, [2]Laboratory for Atmospheric and Space Physics, University of Colorado, Boulder, CO, USA, [3]Ionospheric Physics, Stoughton, MA, USA

Abstract We conduct observational and modeling studies of thermospheric composition responses to weak geomagnetic activity (nongeomagnetic storms). We found that the thermospheric O and N$_2$ column density ratio ($\sum$O/N$_2$) in part of the Northern Hemisphere measured by Global-scale Observations of the Limb and Disk (GOLD) exhibited large and long-lived depletions during weak geomagnetic activity in May and June 2019. The depletions reached 30% of quiet time values, extended equatorward to 10°N and lasted more than 10 hr. Furthermore, numerical simulation results are similar to these observations and indicate that the $\sum$O/N$_2$ depletions were pushed westward by zonal winds. The $\sum$O/N$_2$ evolution during weak geomagnetic activity suggests that the formation mechanism of the $\sum$O/N$_2$ depletions is similar to that during a geomagnetic storm. The effects of weak geomagnetic activity are often ignored but, in fact, are important for understanding thermosphere neutral composition variability and hence the state of the thermosphere-ionosphere system.

Plain Language Summary The column density ratio of O and N$_2$ ($\sum$O/N$_2$) has been used to monitor geomagnetic storm effects in the thermosphere, as well as providing valuable information about the ionosphere. This triggers an important question: Can weak geomagnetic activities cause changes in thermospheric composition too? Here, we conduct studies based on geostationary orbit observations and numerical simulations. Model outputs replicate the general morphology of this variability for the cases examined. This made it possible to understand the cause of the composition response to weak geomagnetic forcing. We found that the $\sum$O/N$_2$ depletion observed was pushed westward by the zonal wind. During weak geomagnetic activity, the $\sum$O/N$_2$ response is similar to the response during a geomagnetic storm, albeit it is weaker. In summary, our study suggests that weak geomagnetic activity can also generate strong and long-lived responses in thermosphere composition during solar minimum and that this response can be important to understanding the thermosphere and ionosphere variability during the so-called quiet times.

1. Introduction

The response of thermosphere composition to geomagnetic storms has been investigated for several decades since the first study carried out by Seaton (1956). Based on the observations from Satellite-Borne Gas Analyzers, Prölss (1980, 1981) summarized how geomagnetic storms influence the distribution of neutral species in the thermosphere. They found that the composition disturbances were restricted to high latitudes in the later afternoon and evening sectors, and the maximum disturbances occurred near the boundary of the auroral zone. The perturbed neutral composition was also found to expand toward midlatitude and even low latitude in the night and early morning sectors. In the early morning sector, there are seasonal variations of the extended composition disturbance zone in midlatitude and low latitude. These initial findings have since been validated by a number of observational and modeling studies (e.g., Burns et al., 1991, 1995, 2004; Fuller-Rowell et al., 1994, 1996).

The column density ratio of atomic oxygen (O) to molecular nitrogen (N$_2$) ($\sum$O/N$_2$) is an important parameter in the thermosphere that can be derived from the observed O 135.6 nm and N$_2$ Lyman-Birge-Hopfield (LBH) radiances (Strickland et al., 1995, 1999, 2001). $\sum$O/N$_2$ is obtained by integrating densities of O and N$_2$ from infinity down to an altitude where the column number density of N$_2$ is 1×10^{17}/cm^2, and thus, it is actually defined on a constant pressure surface with no altitude information

(Correira et al., 2020). O and N_2 number densities decrease exponentially with altitude, so the column number densities of O and N_2 at the altitude where the N_2 column number density is $1 \times 10^{17}/cm^2$ is mainly from altitudes immediately above this level (approximately 140–180 km). This altitude region encompasses most of LBH radiance and minimizing the uncertainty in $\sum O/N_2$ as a function of 135.6 nm/LBH. In this paper, we use 160 km to represent this low-middle-thermosphere region.

Understanding thermospheric composition variations, especially those of O and N_2, is important for space weather research and applications. For instance, O and N_2 are the major components of the thermosphere, influencing the total mass density of the thermosphere, which is important for monitoring and predicting the orbits of near-Earth satellites (Emmert, 2009). Furthermore, $\sum O/N_2$ can also be used to represent thermosphere composition and total mass density changes due to geomagnetic storms (Crowley et al., 2006; Lei et al., 2010; Liu et al., 2020; Yuan et al., 2015; Zhang et al., 2003). $\sum O/N_2$ is also important for understanding the variability in the ionosphere (Liou et al., 2005; Lu et al., 2012; Zhang et al., 2003) since it reflects the production and loss of the ionospheric F-region plasma (Rishbeth, 1998).

Burns et al. (2004) investigated the responses of N_2 to geomagnetic storms with the same strength during solar minimum and solar maximum in the upper thermosphere (around 300 km). Their results showed that the same strength geomagnetic storm would exert relatively stronger effects on the thermosphere (compared with quiet time background conditions) during solar minimum than it did during solar maximum. This is due to less solar energy input during solar minimum. Their study triggered a series of questions: Will the neutral composition in the upper or even middle thermosphere also respond to the geomagnetic activity that is weaker than a geomagnetic storm (defined as global geomagnetic activity index (Kp) $\geq$ 5, from https://www.swpc.noaa.gov/noaa-scales-explanation) during solar minimum? If yes, how strong is the response? And, is the response in composition similar to or different from that during geomagnetic storms? Previous studies have provided some empirical connections between thermosphere mass density and Kp based on the measurements from low-Earth orbiting (LEO) satellites (Lei et al., 2008; Qian & Solomon, 2011). However, LEO satellites can only provide cross-track scanned images or profiles at certain local times (LTs) near the orbit, which results in gaps in information on the spatial and temporal variability of the composition. This impedes a full understanding of how $\sum O/N_2$ responds to geomagnetic activity, either weak or strong, over a large area and the physical mechanisms that are driving this response.

There have been some previous satellite observations that provided two-dimensional (2D) imaging of $\sum O/N_2$, such as Polar (Liou et al., 2005) and IMAGE (Zhang et al., 2003) satellites; however, the studies of $\sum O/N_2$ response to geomagnetic activity using these data are rare. Furthermore, previous studies reported some cases of ionospheric and thermospheric variations that might be associated with weak geomagnetic activity (e.g., Goncharenko et al., 2006; Zhao et al., 2008). However, there have not been quantitative studies on whether there are observable variations in thermosphere composition due to weak geomagnetic activity and how weak this activity can be. On the other hand, as shown by Rishbeth (1998), daytime ionospheric F-region electron densities correlate well with thermospheric O/N_2 ratio. Understanding the O/N_2 response to weak geomagnetic activity conditions is thus of great importance in quantitatively describing ionospheric plasma density variations and investigating the physical processes.

The 2D synoptic imaging of $\sum O/N_2$ provided by the Global-scale Observations of the Limb and Disk (GOLD) mission in geostationary orbit allows for a 2D study on the middle thermosphere composition response to weak geomagnetic activity during solar minimum from high latitudes to the equator in the American and Atlantic longitude sectors. In this paper, we report three typical cases of the $\sum O/N_2$ response to weak geomagnetic activity. Furthermore, the $\sum O/N_2$ simulated by the National Center for Atmospheric Research (NCAR) Thermosphere-Ionosphere Electrodynamics General Circulation Model (TIE-GCM) displayed a similar pattern in these cases. This similarity between the observations and model simulations makes it possible to carry out in-depth diagnostic investigations of the underlying physical mechanisms of the $\sum O/N_2$ response. The remainder of the paper is organized as follows. Section 2 describes the observations and numerical model. Section 3 provides three typical cases with depleted $\sum O/N_2$ in the Northern Hemisphere during weak geomagnetic activity observed by GOLD. Section 4 describes the data-model comparison. Section 5 gives the discussion, and the conclusions are presented in section 6.

2. Data and Model

2.1. GOLD Data

GOLD flies onboard the SES-14 communication satellite, which was launched on 25 January 2018. The satellite is located in a geostationary orbit over 47.5°W. The only scientific instrument onboard is the GOLD Far Ultraviolet (FUV) imager, which performs measurements in the FUV (Eastes et al., 2020, 2017). As the instrument makes measurements from geostationary orbit, GOLD provides images of the same region (over $120° \times 140°$) in a similar universal time (UT) range every day. It observes Earth's daytime airglow emissions from 134 to ~162 nm with a spectral resolution of 0.02 nm, including the OI 135.6 nm and N_2 LBH bands from 140.0 to 150.0 nm during the daytime (Eastes et al., 2017). $\sum O/N_2$ is derived from the daytime OI 135.6 nm and the N_2 LBH brightness. For the daytime mode, the GOLD imager scans the full disk at a 30-min cadence with a longitude range from 120°W to 20°E and a latitude range from 70°S to 70°N. In this study, we utilized the GOLD observed $\sum O/N_2$ in the Northern Hemisphere with a spatial resolution of $1° \times 1°$. The data are smoothed by a $5° \times 5°$ moving window in latitude and longitude to remove small-scale perturbations. The measurement errors of the $\sum O/N_2$ data we used in this study are 5–10%.

### 2.2. Thermosphere-Ionosphere Electrodynamics General Circulation Model

The TIE-GCM is a first principles upper atmosphere general circulation model that solves the continuity, momentum, energy, and electrodynamic equations of the coupled thermosphere-ionosphere (TI) system (Qian et al., 2014; Richmond et al., 1992; Roble et al., 1988). It utilizes a spherical coordinate system fixed with respect to the rotating Earth, with latitude and longitude as the horizontal coordinates and pressure surfaces as the vertical coordinate. The pressure surface is defined as $\ln P_0/P$, where $P_0 = 5 \times 10^{-7}$ Pa is the reference level. The vertical range of the model is about 97–600 km, depending on solar activity. In this study, we run the TIE-GCM 2.0 using the Weimer empirical model (Weimer, 2005) to provide the high-latitude inputs. The spatial resolution is $2.5° \times 2.5° \times 0.25$ scale heights. The model step is 30 s, and the output data are saved every 30 min at 10th and 40th minute at every UT. These times have been selected to match with the UTs when GOLD images the Northern Hemisphere.

3. Observational Results

To determine $\sum O/N_2$ variations in weak geomagnetic activity events, we employed the following criteria. First, we searched for 2 consecutive geomagnetically quiet days. The quiet days are determined mainly based on the Auroral electrojet (AE) index and Kp. The AE index was required to be less than or equal to 250 nT during the whole day, or between 250 and 500 nT for less than 1 hr. And the daily averaged Kp had to be less than or equal to 1. If the third day (or even both the third and fourth days) had weak geomagnetic activity (both 1 < Kp < 5 and 250 < AE < 1,000 nT lasting for at least 3 hr), these 3 or 4 days satisfied our definition of a weak geomagnetic activity event. Using the second day as the reference quiet day, we subtract the second day results from other 3 days and then divide the differences with the second-day, quiet-time values to obtain the percentage difference (% Diff) of $\sum O/N_2$ at a particular UT between other 3 days and the second day. We do not choose the first day as reference to avoid any contaminations from possible geomagnetic disturbances occurring on the day before the first day.

The top left panel in Figure 1 shows the AE index between DOY 145 and 148 (25 and 28 May) in 2019. The corresponding Kp and disturbance storm time (Dst) indices are shown in the left panel of Figure S1. Kp and Dst have a 1-hr resolution (3-hr Kp is interpolated into 1 hr on the OMNI website), and the AE index has a 1-min resolution and is smoothed by a 10-min window. The AE index on DOY 145 and 146 was low (<250 nT) and these 2 days are regarded as quiet days. AE then increased to ~750 nT at 8 UT on DOY 147, and this disturbance continued until 20 UT when it decreased to less than 250 nT. Kp was 0.3 during most of the time on DOY 145 and 146. It suddenly increased from 0.3 to 3 from 18 to 21 UT on DOY 146. Dst was mostly positive on DOY 145 and 146. It suddenly decreased from 16 to −1 nT around 7 UT on DOY 147 and finally reached a minimum of −16 nT at 21 UT on the same day. Based on the evolution of AE, Kp, and Dst, we can see that there was a weak geomagnetic disturbance appearing around 8 UT and ending near 20 UT on DOY 147.

The second and third subplots of the first column of Figure 1 show the percentage difference of $\sum O/N_2$ at 13:10 UT between the two quiet days (middle) and between the disturbed and quiet days (bottom) for the
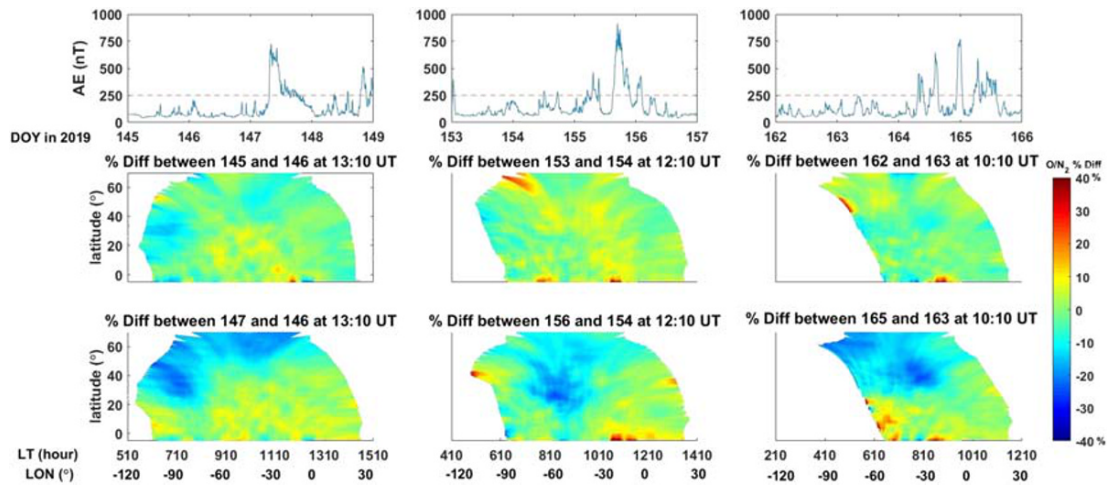
Figure 1. (First row) The AE indices for three cases (DOY 145–148; DOY 153–156; DOY 162–165 in 2019); (second row) the percentage differences of $\sum O/N_2$ between the two quiet days in the three cases; (third row) the percentage differences between the disturbed and quiet days. The longitude and the corresponding local time are given as the x-axis. The red line is 250 nT.

weak geomagnetic activity on DOY 147. We can see that the $\sum O/N_2$ percentage difference between DOY 145 and 146 only exhibited a small region with a maximum depletion of -15% (90–110°W, 30–35°N). On the other hand, the $\sum O/N_2$ percentage difference between DOY 147 and 146 exhibited a large region with a maximum depletion of -23%. This large depletion region was mainly distributed in the early morning and noon sectors. The earlier LT depletion penetrated southward, reaching mid-low latitudes (~20°N). By checking the time series of the percentage difference of $\sum O/N_2$ (see Movie S1), we found that the observed depletion region appeared at 8:10 UT in the GOLD field of view (FOV) and moved toward local early morning and afternoon sectors. It also extended equatorward to ~20°N before 13:40 UT. Then, it gradually shrank back to 45°N at 17:40 UT but again expanded latitudinally after 19:10 UT, reaching ~35°N until the observation period ended at 22:40 UT. The maximum depletion (percentage difference) reached -30%.

We found two additional cases in 2019 that meet the selection criteria. One is from DOY 153 to 156 (2–5 June). DOY 153 and 154 were quiet days, and DOY 155 and 156 were disturbed days (hereafter Case 2). Another is from DOY 162–165 (11–14 June). DOY 162 and 163 were quiet days, and DOY 164 and 165 were disturbed days (hereafter Case 3). As shown in the top middle panel in Figures 1 and S1, the geomagnetic disturbance of Case 2 began at 15 UT on DOY 155 and continued to 3 UT on DOY 156, with a maximum Kp of 2.3, AE of 900 nT and a minimum Dst of -25 nT. Although there were several AE peaks over 250 nT on DOY 153 and 154, their durations were less than 1 hr, and therefore, DOY 153 and 154 were still regarded as quiet days. Case 3 is shown in the top right panel of Figures 1 and S1. In this case, several geomagnetic disturbances occurred after 7 UT on DOY 164 and finally ended at 15 UT on DOY 165. The maximum AE and Kp were 770 nT and 4, respectively, and minimum Dst was -12 nT. The $\sum O/N_2$ percentage differences between quiet and disturbed times in Cases 2 and 3 are shown at different UTs from Case 1 due to the different onset times of the geomagnetic disturbances. For the percentage difference between the disturbed and quiet times at 12:10 UT in Case 2, there was a region of $\sum O/N_2$ depletion between 40°W and 75°W, 10°N and 50°N with a maximum depletion of -25%. For the percentage difference between the disturbed and quiet times at 10:10 UT in Case 3, $\sum O/N_2$ depletion occurred between 20°W and 80°W, 30°N and 70°N with a maximum depletion of -25%. It should be noted that for Case 2, Figure 1 shows the percentage difference between DOY 156 and 154 not DOY 155 and 154 because there was only depletion near the upper edge of the GOLD scanned region (60–70°N, 70–90°W with larger measurement error) after 20:40 UT on DOY 155. However, the $\sum O/N_2$ depletion appeared and extended to mid-low latitudes (as low as 10°N) after the end of the geomagnetic disturbance at 3 UT on DOY 156. The depletion continued during the whole observation period (6:10–22:40 UT: 3–19 hr after the geomagnetic disturbance ended) in the GOLD scanned region (see Movie S2). Likewise, for Case 3, Figure 1 shows the percentage difference between DOY 165 and 163, because there was no $\sum O/N_2$ depletion on DOY 164 seen in the GOLD scanned region. The depletion of
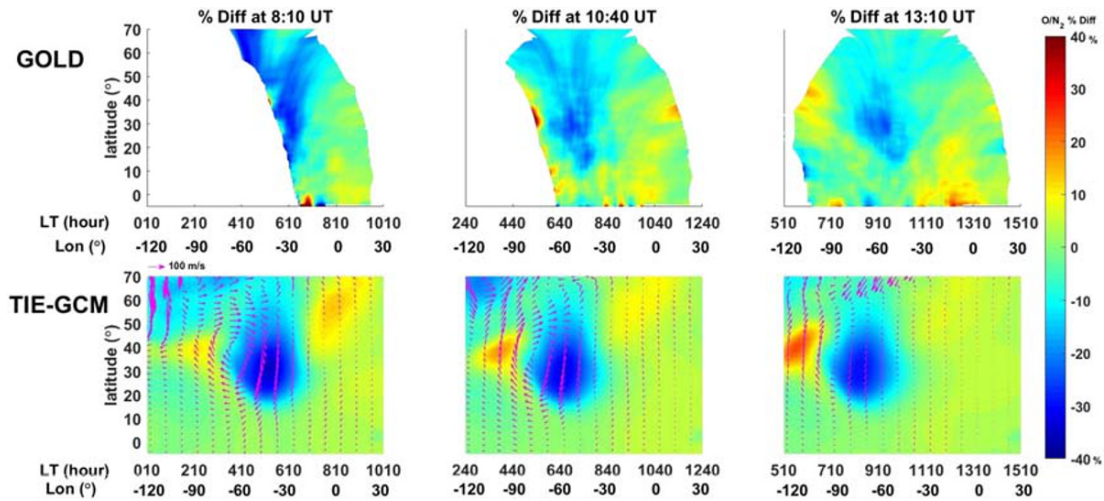
Figure 2. Latitude-longitude distribution of the percentage differences between DOY 156 and 154 in (first row) GOLD observations and (second row) TIE-GCM simulations with neutral wind differences vectors (pink) at pressure level −1.375 (~160 km). The longitude and the corresponding local time are given as the *x*-axis.

$\sum O/N_2$ on DOY 165 was relatively weaker (−15% to −20%) compared with those in Cases 1 and 2, and so was the AE index. For the percentage difference between DOY 165 and 163, the depletion was apparent beginning from 6:40 UT (approximately −20%) and almost disappeared after 13:40 UT, though the geomagnetic disturbance continued until 15 UT on DOY 165. Since the GOLD observations do not cover 70–90°N, it is difficult to know whether there was a depletion in the high latitude region. In all, these three cases suggest that $\sum O/N_2$ in the Northern Hemisphere (North America and Atlantic Ocean) exhibits strong responses (maximum depletion −30%, penetrating equatorward to ~10°N) on the dayside to weak geomagnetic disturbances ($1 < Kp < 5$, $250 < AE < 1,000$ nT). And they can last long after the disturbance ends (>10 hr).

4. Model-Data Comparison

In the following, we use the TIE-GCM simulations to understand the formation and evolution of the observed daytime $\sum O/N_2$ depletion. The reference altitude of N_2 column density of $10^{17}/cm^2$ in the model is around 135–140 km. The model shows similar $\sum O/N_2$ depletion to the observations for all the cases. Here, we use the percentage difference between DOY 156 and 154 in Case 2 as an example, as the simulated $\sum O/N_2$ was closest to the observations (GOLD and TIE-GCM comparison for the two other cases are given in Figure S2). Figure 2 shows the comparisons of the percentage difference between DOY 156 and 154 in the TIE-GCM simulations and GOLD observations at 8:10, 10:40, and 13:10 UT. Both exhibit $\sum O/N_2$ depletion in mid-low latitudes (15–50°N). Although there are some quantitative differences, such as the 5–10° wider longitude range, larger magnitude of the simulated $\sum O/N_2$ depletion (5–10% more than observed) and different westward motion velocities (~160 m/s for simulation and ~50–100 m/s for observation), the basic structures are similar between simulations and observations.

Those model-data discrepancies might be attributed to the thermosphere day-to-day variability caused by lower atmosphere forcing such as planetary wave and tides. Furthermore, the model's high-latitude forcing is based on empirical Weimer model (Weimer, 2005), which can be very different from the actual forcing. The similarity between the observations and simulations indicates that the TIE-GCM can be used to uncover the formation mechanisms of the daytime $\sum O/N_2$ depletion due to weak geomagnetic activity and its long duration. The bottom panels of Figure 2 show the neutral wind differences vectors (pink) at the model pressure level $z = -1.375$ (near altitude around 160 km) on DOY 156. Westward zonal wind differences (approximately −70 m/s) were dominant near the west edge of the $\sum O/N_2$ depletion, whereas the equatorward meridional wind difference was strong inside the $\sum O/N_2$ depletion. From 8:10 to 13:10 UT, the wind differences decreased, but the depletion region kept moving westward. The behavior of neutral wind difference

and the westward motion of $\sum O/N_2$ depletion suggest the possible important role of the horizontal wind, which will be investigated in next section.

5. Discussion

Diagnostic analysis of the O continuity equation (Burns et al., 1989) has been carried out to obtain insight into the formation and development of daytime $\sum O/N_2$ depletions at middle and low latitudes. $\sum O/N_2$ occurs approximately on a constant pressure surface. Thus, thermal expansion and contraction do not affect it because they merely move the pressure surface up and down.

Figure S3 shows the latitude-longitude distribution of the difference of vertical advection (dVAO), meridional advection (dHAOV), zonal advection (dHAOU), and molecular diffusion (dDOME) between DOY 154 and 156 at pressure level −1.375 at 8:10 UT. As shown in Figure S3, zonal advection was the dominant process for the westward motion of the $\sum O/N_2$ depletion region, as compared to other processes. The time series of the term analysis of O at pressure level −1.375 on DOY 156 (see Movie S3) also shows that zonal advection dominates the westward motion of $\sum O/N_2$ after the ending of weak geomagnetic activity on DOY 156 (after 3 UT). In the following, we investigate the time evolution of the $\sum O/N_2$ depletion during the geomagnetic disturbance to understand how this depletion was formed and whether the formation process was similar to that which occurred during geomagnetic storms.

As mentioned earlier, the geomagnetic disturbance in Case 2 started at around 15 UT on DOY 155 and continued until 3 UT on DOY 156 with a maximum AE of 900 nT and Kp of 2.3. We focus on the time before the beginning of GOLD observations on DOY 156 (6:10 UT) to investigate how the $\sum O/N_2$ depletion was formed. Figure 3 shows the latitude-longitude distribution of $\sum O/N_2$ percentage difference on DOY 155 (17:10–23:10 UT) and 156 (2:10–6:10 UT). When the geomagnetic disturbance began, the model-calculated vertical winds increased greatly (4 m/s at model pressure level $z = −1.375$) near 60–80°N between 1–3 LT due to the temperature changes caused by Joule heating (not shown here). The upward vertical winds led to a reduction in $\sum O/N_2$ in the high-latitude thermosphere. Then ion-neutral coupling drove strong meridional winds which carried the O/N_2 -depleted air equatorward (Mayr et al., 1978; Prölss, 1980). Figure 3a shows a weak depletion near 21–1 LT in the high latitudes (70–90°N). Then, this depletion became stronger and expanded equatorward, as well as toward midnight and the early morning sectors (from 21 LT at 17:10 UT to 22 LT at 20:10 UT and to 2:10 LT at 23:10 UT, as shown in Figures 3b and 3c). It is interesting to notice that there were already some depletions in the midlatitudes (near 5:10 LT at 17:10 UT) even before the commencement of the geomagnetic activity at 15 UT on DOY 155, which will be studied in later work. The neutral wind differences in the depletion region (not shown) also had a large equatorward component (around −100 to −200 m/s). On DOY 156, the depletion structure kept expanding equatorward to midlatitude and lowlatitude until 4:10 UT (Figures 3d–3e). It subsequently moved slowly westward, as shown in Figure 3f. This is similar to the observed $\sum O/N_2$ depletion seen by GOLD after 7:40 UT. The time evolution of the $\sum O/N_2$ depletion structure and the underlying physical mechanism inferred from Figure 3 agree with the concept proposed by Prölss (1980, 1981). In particular, the disturbance region of neutral species due to the geomagnetic storm corotated toward the local early morning or even the noon side from the local nightside. Therefore, the behavior of the $\sum O/N_2$ response in the Northern Hemisphere to weak geomagnetic activity during solar minimum is similar to what occurs during geomagnetic storms. This is clearly demonstrated by both observations and model simulations in this paper.

Furthermore, several previous studies reported observations (de La Beaujardiere et al., 2009) or simulations (Liu et al., 2010) of electron density depletions during geomagnetically quiet conditions (Kp ≤ 4). They attributed these depletions to the lower atmosphere (below 80 km) forcing such as planetary waves and tides. From GOLD observations and the close relationship between electron density and O/N_2 in the middle latitudes, electron density depletions seen under these conditions thus may not be entirely due to the lower atmosphere forcing. Weak geomagnetic activity can play a crucial role in forming the depletions and their subsequent evolutions. Understanding the O/N_2 variations and their associated plasma density variations in the ionosphere is of great importance.

In support of these three case studies, we also looked for other similar events that satisfied the aforementioned criteria. There were 25 cases of weak geomagnetic activity events between 1 October 2018 and 31
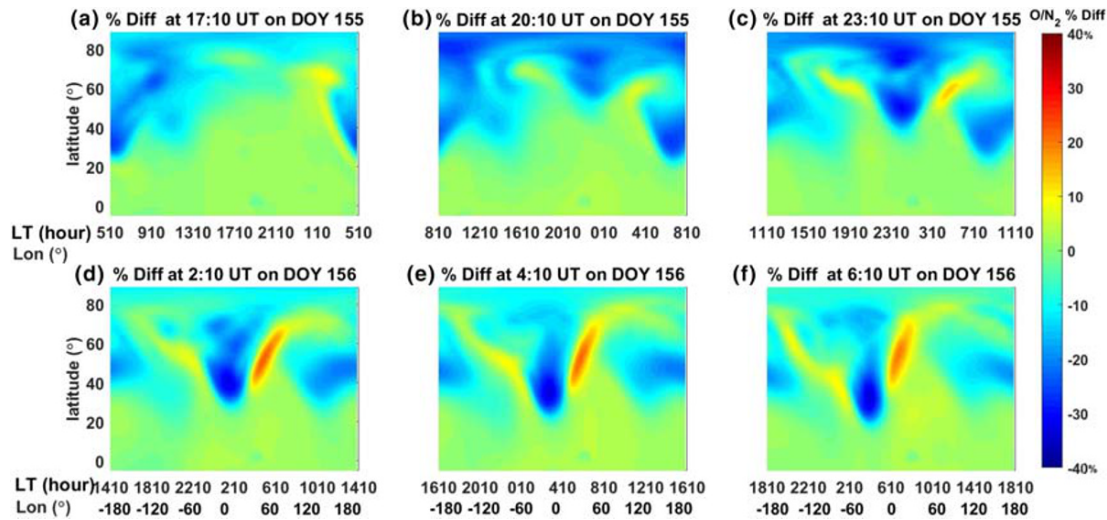
Figure 3. Latitude-longitude distribution of $\sum O/N_2$ percentage differences between the disturbed and quiet times on (a–c) DOY 155 and (d–f) 156 before GOLD observations.

December 2019 that met these criteria. More than 70% of them were associated with $\sum O/N_2$ depletions. The duration of that daytime $\sum O/N_2$ depletions was longer than 4 hr in these cases. The strong and long-lived $\sum O/N_2$ depletions seen in the three cases are therefore common in the thermosphere under weak geomagnetic activity conditions. It is also interesting to notice that there were no apparent $\sum O/N_2$ depletions in the northern winter hemisphere during the December solstice. Depletions appeared in the southern summer hemisphere instead.

The time difference between the geomagnetic disturbance onset and the time when the depletion appeared in the GOLD FOV can vary from 3 hr to more than 12 hr. The possible causes of these different response times are an interesting topic for future study.

6. Conclusion

We reported that GOLD observed Northern Hemisphere $\sum O/N_2$ responses to weak geomagnetic activity ($1 < Kp < 5$ and $250 < AE < 1,000$ nT) and investigated their formation and propagation mechanisms using the NCAR TIE-GCM. Our main findings are summarized as follows:

1. The Northern Hemisphere $\sum O/N_2$ was depleted during and after weak geomagnetic disturbances under solar minimum "quiet" conditions. The maximum depletion reached -30% and expanded equatorward to 10°N.
2. The depletions of the Northern Hemisphere $\sum O/N_2$ during weak geomagnetic disturbances can persist for a long time (more than 10 hr), even after the end of the disturbances.
3. TIE-GCM simulations show similar $\sum O/N_2$ depletion patterns. The depletions were first formed mainly by strong vertical winds and then pushed equatorward by the meridional winds in the nighttime. The depletion region subsequently corotated into the early morning and noon sectors. It then slowly moved westward, mainly driven by the westward zonal winds.
4. The behavior of the neutral composition response to weak geomagnetic disturbances is similar to that which occurs during geomagnetic storms.
5. This paper demonstrates that weak geomagnetic activity plays an important role in the variations of thermosphere composition during solar minimum "quiet" conditions.

Data Availability Statement

The GOLD data are available from http://gold.cs.ucf.edu/. The Auroral electrojet index data are from http://supermag.jhuapl.edu/. The Kp and Dst data are from https://omniweb.gsfc.nasa.gov/form/dx1.html. The TIE-GCM simulation results used to produce this paper are available at https://doi.org/10.5065/7dvt-rm26.

Geophysical Research Letters

References

Burns, A. G., Killeen, T. L., Deng, W., Carignan, G. R., & Roble, R. G. (1995). Geomagnetic storm effects in the low- and middle-latitude upper thermosphere. *Journal of Geophysical Research*, *100*(A8), 14,673–14,691. https://doi.org/10.1029/94JA03232

Burns, A. G., Killeen, T. L., & Roble, R. G. (1989). Causes of changes in composition calculated using a thermospheric general circulation model. *Journal of Geophysical Research*, *94*(A4), 3670–3686. https://doi.org/10.1029/JA094iA04p03670

Burns, A. G., Killeen, T. L., & Roble, R. G. (1991). A simulation of thermospheric composition changes during an impulse storm. *Journal of Geophysical Research*, *96*(A8), 14,153–14,167. https://doi.org/10.1029/91JA00678

Burns, A. G., Wang, W., Killeen, T. L., & Roble, R. G. (2004). The solar cycle-dependent response of the thermosphere to geomagnetic storms. *Journal of Atmospheric and Solar - Terrestrial Physics*, *66*(1), 1–14. https://doi.org/10.1016/j.jastp.2003.09.015

Correira, J., Evans, J. S., Krywonos, A., Lumpe, J. D., Veibell, V., McClintock, W. E., & Eastes, R. W. (2020). Thermospheric composition and solar EUV flux from the Global-scale Observations of the Limb and Disk (GOLD) mission. *Earth and Space Science Open Archive*, *36*. https://doi.org/10.1002/essoar.10501920.1

Crowley, G., Hackert, C. L., Meier, R. R., Strickland, D. J., Paxton, L. J., Pi, X., et al. (2006). Global thermosphere-ionosphere response to onset of 20 November 2003 magnetic storm. *Journal of Geophysical Research*, *111*, A10S18. https://doi.org/10.1029/2005JA011518

de La Beaujardiere, O., Retterer, J. M., Pfaff, R. F., Roddy, P. A., Roth, C., Burke, W. J., et al. (2009). C/NOFS observations of deep plasma depletions at dawn. *Geophysical Research Letters*, *36*, L00C06. https://doi.org/10.1029/2009GL038884

Eastes, R. W., McClintock, W. E., Burns, A. G., Anderson, D. N., Andersson, L., Aryal, S., et al. (2020). Initial observations by the Global-scale Observations of the Limb and Disk (GOLD) mission. *Journal of Geophysical Research: Space Physics*, *125*, e2020JA027823. https://doi.org/10.1029/2020JA027823

Eastes, R. W., McClintock, W. E., Burns, A. G., Anderson, D. N., Andersson, L., Codrescu, M., et al. (2017). The Global-Scale Observations of the Limb and Disk (GOLD) mission. *Space Science Reviews*, *212*(1–2), 383–408. https://doi.org/10.1007/s11214-017-0392-2

Emmert, J. T. (2009). A long-term data set of globally averaged thermospheric total mass density. *Journal of Geophysical Research*, *114*, A06315. https://doi.org/10.1029/2009JA014102

Fuller-Rowell, T. J., Codrescu, M. V., Moffett, R. J., & Quegan, S. (1994). Response of the thermosphere and ionosphere to geomagnetic storms. *Journal of Geophysical Research*, *99*(A3), 3893–3914. https://doi.org/10.1029/93JA02015

Fuller-Rowell, T. J., Codrescu, M. V., Rishbeth, H., Moffett, R. J., & Quegan, S. (1996). On the seasonal response of the thermosphere and ionosphere to geomagnetic storms. *Journal of Geophysical Research*, *101*(A2), 2343–2353. https://doi.org/10.1029/95JA01614

Goncharenko, L., Salah, J., Crowley, G., Paxton, L. J., Zhang, Y., Coster, A., et al. (2006). Large variations in the thermosphere and ionosphere during minor geomagnetic disturbances in April 2002 and their association with IMF B_y. *Journal of Geophysical Research*, *111*, A03303. https://doi.org/10.1029/2004JA010683

Lei, J., Thayer, J. P., Burns, A. G., Lu, G., & Deng, Y. (2010). Wind and temperature effects on thermosphere mass density response to the November 2004 geomagnetic storm. *Journal of Geophysical Research*, *115*, A05303. https://doi.org/10.1029/2009JA014754

Lei, J., Thayer, J. P., Forbes, J. M., Sutton, E. K., & Nerem, R. S. (2008). Rotating solar coronal holes and periodic modulation of the upper atmosphere. *Geophysical Research Letters*, *35*, L10109. https://doi.org/10.1029/2008GL033875

Liou, K., Newell, P. T., Anderson, B. J., Zanetti, L., & Meng, C.-I. (2005). Neutral composition effects on ionospheric storms at middle and low latitudes. *Journal of Geophysical Research*, *110*, A05309. https://doi.org/10.1029/2004JA010840

Liu, H.-L., Wang, W., Richmond, A. D., & Roble, R. G. (2010). Ionospheric variability due to planetary waves and tides for solar minimum conditions. *Journal of Geophysical Research*, *115*, A00G01. https://doi.org/10.1029/2009JA015188

Liu, J., Burns, A. G., Wang, W., & Zhang, Y. (2020). Modelled IMF B_y effects on the polar ionosphere and thermosphere coupling. *Journal of Geophysical Research: Space Physics*, *125*, e2019JA026949. https://doi.org/10.1029/2019JA026949

Lu, G., Goncharenko, L., Nicolls, M. J., Maute, A., Coster, A., & Paxton, L. J. (2012). Ionospheric and thermospheric variations associated with prompt penetration electric fields. *Journal of Geophysical Research*, *117*, A08312. https://doi.org/10.1029/2012JA017769

Mayr, H. G., Harris, I., & Spencer, N. W. (1978). Some properties of upper atmosphere dynamics. *Reviews of Geophysics*, *16*(4), 539–565. https://doi.org/10.1029/RG016i004p00539

Prölss, G. W. (1980). Magnetic storm associated perturbation of the upper atmosphere: Recent results obtained by satellite-borne gas analyzers. *Reviews of Geophysics*, *18*(1), 183–202. https://doi.org/10.1029/RG018i001p00183

Prölss, G. W. (1981). Latitudinal structure and extension of the polar atmospheric disturbance. *Journal of Geophysical Research*, *86*(A4), 2385–2396. https://doi.org/10.1029/JA086iA04p02385

Qian, L., Emery, B. A., Foster, B., Lu, G., Maute, A., Richmond, A. D., et al. (2014). The NCAR TIE-GCM: A community model of the coupled thermosphere/ionosphere system. In J. Huba, R. Schunk, & G. Khazanov (Eds.), *Modeling the ionosphere- thermosphere system* (pp. 73–83). Chichester, UK.: John Wiley.

Qian, L., & Solomon, S. C. (2011). Thermospheric density: An overview of temporal and spatial variations. *Space Science Reviews*, *168*(1–4), 147–173. https://doi.org/10.1007/s11214-011-9810-Z

Richmond, A. D., Ridley, E. C., & Roble, R. G. (1992). A thermosphere/ionosphere general circulation model with coupled electrodynamics. *Geophysical Research Letters*, *19*(6), 601–604. https://doi.org/10.1029/92GL00401

Rishbeth, H. (1998). How the thermospheric circulation affects the ionospheric F_2-layer. *Journal of Atmospheric and Terrestrial Physics*, *60*(14), 1385–1402. https://doi.org/10.1016/S1364-6826(98)00062-5

Roble, R. G., Ridley, E. C., Richmond, A. D., & Dickinson, R. E. (1988). A coupled thermosphere/ionosphere general circulation model. *Geophysical Research Letters*, *15*(12), 1325–1328. https://doi.org/10.1029/GL015i012p01325

Seaton, M. J. (1956). A possible explanation of the drop in F-region critical densities accompanying major ionospheric storms. *Journal of Atmospheric and Terrestrial Physics*, *8*(1–2), 122–124. https://doi.org/10.1016/0021-9169(56)90102-7

Strickland, D. J., Bishop, J., Evans, J. S., Majeed, T., Shen, P. M., Cox, R. J., et al. (1999). Atmospheric Ultraviolet Radiance Integrated Code (AURIC): Theory, software architecture, inputs, and selected results. *Journal of Quantitative Spectroscopy & Radiative Transfer*, *62*(6), 689–742. https://doi.org/10.1016/S0022-4073(98)00098-3

Strickland, D. J., Daniell, R. E., & Craven, J. D. (2001). Negative ionospheric storm coincident with DE-1 observed thermospheric disturbance on October 14, 1981. *Journal of Geophysical Research*, *106*(A10), 21,049–21,062. https://doi.org/10.1029/2000JA000209

Strickland, D. J., Evans, J. S., & Paxton, L. (1995). Satellite remote sensing of thermospheric O/N2 and solar EUV: 1. Theory. *Journal of Geophysical Research*, *100*(A7), 12,217–12,226. https://doi.org/10.1029/95JA00574

Weimer, D. R. (2005). Improved ionospheric electrodynamic models and application to calculating joule heating rates. *Journal of Geophysical Research*, *110*, A05306. https://doi.org/10.1029/2004JA010884

Yuan, T., Zhang, Y., Cai, X., She, C.-Y., & Paxton, L. J. (2015). Impacts of CME induced geomagnetic storms on the midlatitude mesosphere and lower thermosphere observed by a sodium lidar and TIMED/GUVI. *Geophysical Research Letters*, *42*, 7295–7302. https://doi.org/10.1002/2015GL064860

Zhang, Y., Paxton, L. J., Kil, H., Meng, C.-I., Mende, S. B., Frey, H. U., & Immel, T. J. (2003). Negative ionospheric storms seen by the IMAGE FUV instrument. *Journal of Geophysical Research*, *108*, 1343. https://doi.org/10.1029/2002JA009797

Zhao, B., Wan, W., Liu, L., Igarashi, K., Nakamura, M., Paxton, L. J., et al. (2008). Anomalous enhancement of ionospheric electron content in the Asian-Australian region during a geomagnetically quiet day. *Journal of Geophysical Research*, *113*, A11302. https://doi.org/10.1029/2007JA012987